

# Modeling the creep threshold stress due to climb of a dislocation in the stress field of a misfitting precipitate

Matthew E. Krug, David C. Dunand\*

Department of Materials Science and Engineering, Northwestern University, 2220 Campus Drive, Evanston, IL 60208, USA

Received 6 April 2011; accepted 19 April 2011

Available online 3 June 2011

## Abstract

A model for creep threshold stresses in alloys strengthened by coherent, misfitting precipitates is developed for the case where the precipitate is not sheared, and where there are elastic interactions between a dislocation and the precipitate over which it climbs. Calculations of the particle stress field due to a positive stiffness and lattice parameter mismatch between precipitate and matrix predict that the mismatch forces help the dislocation climb/glide process over the precipitates but that they trap it at the departure side of the particle. This results in a true threshold stress, rather than a slowing of the kinetics of dislocation climb as in previous models, which is given by the applied stress necessary to free the dislocation by a glide mechanism. Model predictions and experiment are compared for precipitation-strengthened aluminum alloys containing nanosize  $\text{Al}_3\text{Sc}$ ,  $\text{Al}_3(\text{Sc}, \text{Li})$  and  $\text{Al}_3(\text{Sc}, \text{Yb})$  precipitates with various sizes and mismatches. In agreement with experimental creep results, the model predicts that the threshold stress increases nearly linearly with precipitate radius, and also with the magnitude of the precipitate/matrix lattice mismatch.

© 2011 Acta Materialia Inc. Published by Elsevier Ltd. All rights reserved.

**Keywords:** Creep; Precipitation; Aluminum alloys; Dislocation mobility; High-temperature deformation

## 1. Introduction

A common strategy to improve the high-temperature strength of metals and alloys is to introduce particles [1,2], either coherent precipitates [3–6] or incoherent dispersoids [7–9], which decrease dislocation mobility. In these alloys, when deformation is controlled by matrix dislocations, creep resistance is determined by the rate-limiting process by which dislocations bypass the obstacles. Threshold stresses, below which the creep strain rate is not measurable in a laboratory timeframe, exist for alloys containing coherent precipitates or incoherent dispersoids. When the precipitate is not sheared, these stresses are due to interactions between the dislocations and the particles during climb and bypass [1,2]. For precipitation-strengthened alloys with coherent precipitates, the threshold stress has been attributed to lattice strains induced in the matrix by the precipitates due to a size mismatch that affects the

dislocation climb rate [10,11]; for dispersion-strengthened alloys, electron microscopy observations suggest an attractive interaction between the dislocation and the unsharable, incoherent dispersoid at the detachment side [8,10,12], which occurs after the dislocations have surmounted the obstacles by climb. These mechanisms operate only at elevated temperatures, since dislocation climb requires appreciable rates of vacancy diffusion. The present paper begins with a model developed by Rösler and Arzt [13] for a dislocation climbing around a coherent precipitate, and considers extensions to that model by Marquis and Dunand [11] taking into account matrix misfit strains, resulting in a new model for creep threshold stresses in alloys strengthened by coherent, misfitting precipitates.

## 2. Literature review

### 2.1. Previous models for threshold stresses

Models for threshold stresses in particle-strengthened alloys may be divided into two categories: “local climb”

\* Corresponding author. Tel.: +1 847 491 5370; fax: +1 847 461 6573.  
E-mail address: [dunand@northwestern.edu](mailto:dunand@northwestern.edu) (D.C. Dunand).

models, in which the dislocation follows closely the profile of the particle, inducing a sharp bend where the climbing portion of the dislocation rejoins the glide plane [14,15]; and “general climb” models [16,17], in which portions of the dislocation away from the particle are allowed to relax or “unravel” by diffusion and leave the glide plane, smoothly connecting the portion which is forced to climb over the particle for geometrical reasons to the portions that remain in the glide plane. Threshold stresses predicted for local climb are of the right order of magnitude for dispersion-strengthened alloys (40–70% of the Orowan stress); however, the sharp dislocation bends implied by local climb are unstable high-energy configurations, and therefore unlikely to occur [13,17]. The threshold stresses predicted during general climb, with a dislocation geometry in agreement with transmission electron microscopy (TEM) observations, are much too low however [7,16,18]. Other models of creep threshold stresses in dispersion-strengthened alloys address this discrepancy by postulating attractive interactions between a dislocation and the incoherent dispersoid–matrix interface. Those interactions are due to either diffusional relaxation of dislocation stresses at the interface [9,19,20], or to a reduction in the line energy of dislocations when they become incorporated into the interface [8,21,22].

To explore the discrepancy between experimentally measured threshold stresses and the predictions of general climb models, a model was developed by Rösler and Arzt for threshold stresses in metals with low volume fractions ( $\varphi < \sim 10\%$ ) of non-interacting precipitates (i.e. without departure-side pinning or precipitate shearing) [13]. In this model, the kinetics of general climb of a dislocation over a cubic particle are calculated numerically. Although the model does not yield a closed-form solution for threshold stresses due to general climb, threshold stress values can be determined from computed strain rate vs. stress curves. Using this model, only a small (several per cent) normalized threshold stress, defined as threshold stress divided by the Orowan stress, is predicted; this is well below values observed experimentally in a series of Al–Sc- and Al–Zr-based alloys [4,5,23–31] with a low volume fraction of

nanoscale, coherent precipitates. In the remainder of the present work, we adopt the naming convention introduced in Ref. [13], i.e. the climbing portion and the unraveling portion of the dislocation are called AB and BC, respectively, while portion CD remains in the glide plane, as shown in Fig. 1.

## 2.2. Previous model for threshold stresses due to elastic precipitate–dislocation interactions

The above Rösler–Arzt (R–A) model [13] was extended by Marquis and Dunand (M–D) [11] to consider the effects of elastic interactions between coherent precipitates and dislocations, originating from lattice parameter mismatch and elastic modulus mismatch between the two phases. This extended model comprises a climbing edge dislocation and a cylindrical particle (Fig. 1). A cylinder was chosen to represent the precipitate rather than a sphere or a cube (the latter was used in the R–A model), since an analytical solution exists to describe the shear-modulus mismatch interaction force between a dislocation and an infinitely long cylinder [32,33]. The interaction stress due to a constrained size mismatch  $\varepsilon$  was originally given by Eshelby [34], and the interaction force is obtained through application of the Peach–Koehler equation [35]. In the extended M–D model [11], the equilibrium shape of the climbing dislocation is found by setting equal the chemical potential of a vacancy,  $\mu_v$ , at AB (climbing portion) and at BC (unraveling portion), as was done in the original R–A model [13] (Fig. 1). For the climbing portion AB, the chemical potential of a vacancy is given by:

$$\mu_v = \frac{\frac{\mu_m b^2}{2} \left( \frac{\partial l}{\partial y} \right)_{ABC} - F_c \tan(\beta) - F_g}{\frac{1}{b_2} \frac{dA_{AB}}{dy}} \quad (1)$$

where  $\mu_m$  is the shear modulus of the matrix; the Burgers vector and line sense of the edge dislocation are  $(0 \ \bar{b} \ 0)$  and  $(\bar{1} \ 0 \ 0)$ , respectively;  $(\partial l / \partial y)_{ABC}$  is the derivative of the dislocation length  $l$  with respect to the dislocation glide distance  $y$ , for a constant climb area  $A_{BC}$  between unraveling portion BC and the glide plane;

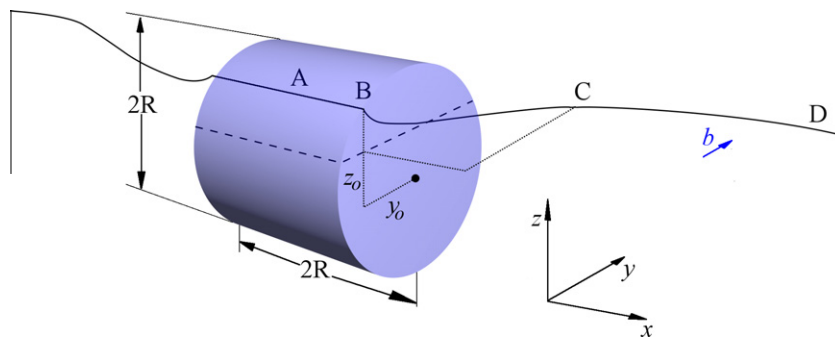


Fig. 1. Schematic of an edge dislocation with Burgers vector  $b$  subjected to a shear stress in the  $y$ -direction, and bypassing by climb a precipitate of diameter and length  $2R$ . A dashed line indicates the glide plane intersection. The dislocation comprises a straight climbing segment, AB, a curved “unraveled” segment, BC, and a curved segment that remains in the glide plane, CD, after Ref. [11]. The coordinate origin resides at the center of the precipitate, but is displaced here for clarity.

$\tan(\beta) = dz/dy$  is the tangent of the dislocation climb trajectory, where  $z$  is the climb direction;  $dA_{AB}/dy$  is the change in climb area  $A_{AB}$  between the climbing portion AB and the glide plane, per unit advance in the glide direction  $y$ ;  $F_c$  and  $F_g$  are the net climb and glide forces acting on the climbing portion AB (Fig. 1).

Using this approach and taking the Al/Al<sub>3</sub>Sc system as an example, Marquis and Dunand [11] calculated creep strain-rate vs. stress curves for Al<sub>3</sub>Sc precipitates of various sizes. The calculated strain rates are in semiquantitative agreement with experimental measurements. The experimental creep curves were not exactly replicated, but their important general features were captured by the extended M–D model. In particular, normalized threshold stresses were predicted to be greater than those for non-interacting precipitates as in the R–A model [13], and to increase with the precipitate radius, unlike the R–A model. The model was additionally applied to ternary Al–Sc–Zr [23] and Al–Mg–Sc [25] alloys. When the lattice parameter mismatch was increased in the model from 0.8% to 1.1% [23], or from 0.74% to 0.91% [25], larger normalized threshold stresses resulted. Predictions from the M–D model that the threshold stress increases with lattice parameter mismatch, for a given precipitate size and volume fraction, were borne out for all Al–Sc–X alloys creep-tested to date. When compared to Al<sub>3</sub>Sc [4,5], Al<sub>3</sub>(Sc,X) show increased mismatch for X = Gd, Yb, Y, Dy or Er [24,30], the same mismatch for X = Zr, Ti and Mg [23,25–29], and decreased mismatch for X = Li [31].

Fig. 2a and b shows contour plots of the dislocation glide and climb forces, respectively, induced in the matrix by a coherent Al<sub>3</sub>Sc precipitate having both lattice parameter and shear modulus mismatch with the matrix; the governing equations (Eqs. (3)–(6) in Ref. [11]) are given in the M–D model article [11]. In this example, which is representative of the general case, the cylindrical precipitate radius  $R$  is 5 nm, and the volume fraction  $\phi$  (necessary for calculating the interprecipitate distance, and therefore the Orowan stress) is 0.0032 (0.32%), which is typical of a dilute Al–0.08 at.% Sc alloy. Distances in the plots have been normalized to  $R$  and the force contours are normalized by the Orowan force,  $f_{Or}$ , which is equal to the Orowan shear stress increment multiplied by the Burgers vector  $b$ , and the interprecipitate distance  $\lambda$  [35]. The Orowan shear stress increment,  $\Delta\sigma_{Or}^c$ , is given by [14,36]:

$$\Delta\sigma_{Or}^c = \frac{0.4\mu_m b}{\pi\sqrt{1-v_m}} \frac{\ln\left(\frac{2-0.82R}{b}\right)}{\lambda} \quad (2)$$

where  $\lambda = R(1.538\phi^{-1/2} - 1.643)$  is the interprecipitate spacing for a volume fraction  $\phi$ , and  $v_m$  is the Poisson's ratio of the matrix. In the present example, the Orowan force is 1.22 nN which, when divided by the Burgers vector and the interprecipitate distance,  $\lambda$ , corresponds to an Orowan stress of 31.3 MPa. For example, in Fig. 2,  $-f_{Or}/16$  indicates a glide force on the climbing dislocation equal in magni-

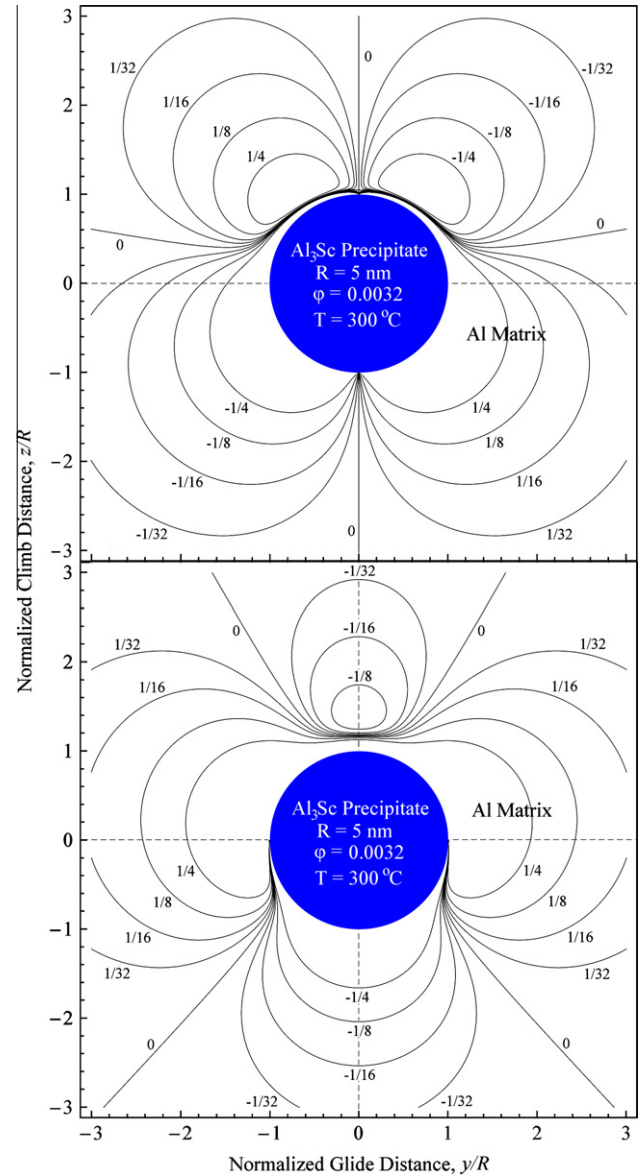


Fig. 2. Glide (top) and climb (bottom) forces, normalized by the Orowan force (calculated from Eq. (2)) on a positive edge dislocation in an Al matrix, due to a misfitting Al<sub>3</sub>Sc precipitate with radius  $R = 5$  nm and volume fraction  $\phi = 0.0032$  at 300 °C.

tude to  $1/16$  of the Orowan force. For an edge dislocation of opposite Burgers vector, the glide forces are mirrored about the line  $z = 0$ , and the climb forces are mirrored about the line  $y = 0$ , resulting in an equivalent stress environment. By reversing the sign of the lattice parameter mismatch, the glide and climb forces are mirrored about the plane  $z = 0$ . An important feature of Fig. 2 is that, due to the elastic interactions, the effective interaction volume of the precipitate with the dislocations is extended into the matrix beyond the geometric volume of the precipitate. In particular, the elastic interactions oppose dislocation glide below  $z/R \approx 0.5$  on the approach side, and above  $z/R \approx 0.5$  on the departure side.

### 3. Present model

#### 3.1. Dislocation trajectories

The M–D model [11] was revisited in the present work, in order to consider further extensions to it. Fig. 3 is adapted from a plot of the glide force contours in Fig. 2 to demonstrate the important features of the model and its refinements. For clarity, the positive glide interaction force contours are removed. Negative glide force contours are the equilibrium trajectories of the climbing portion AB of a positive edge dislocation bypassing the precipitate under a constant applied shear stress  $\tau_{yz}$  applied along the positive direction of the  $y$  axis. Larger applied shear stresses result in a closer approach of the dislocation to the precipitate, to a position where the precipitate-induced glide force counteracts exactly the applied glide force, i.e. where the net glide force is zero. Fig. 3 is shaded to indicate regions where the climb component of the interaction force is positive (assists climb over the precipitate, green) and negative (opposes climb over the precipitate, blue). Red (blue) arrowheads on the three dislocation trajectories shown at the approach side of the precipitate indicate the glide plane height  $z$  where a dislocation climbs over (under) the precipitate, which depends on the sign of the chemical potential of a vacancy. Eq. (3) (presented in Section 3.2)

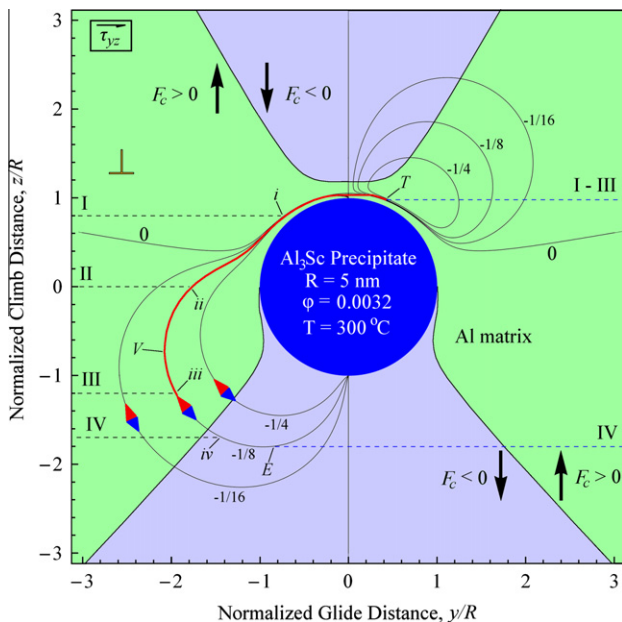


Fig. 3. Contours of negative glide forces—expressed as fractions of the Orowan force (calculated from Eq. (2))—acting on a positive edge dislocation due to a coherent, misfitting  $\text{Al}_3\text{Sc}$  precipitate at  $300\text{ °C}$ . Glide force contours are also dislocation glide/climb trajectories. Contours of zero climb force radiate outward from the precipitate at nearly  $45^\circ$  from  $y = 0$  and  $z = 0$ , and separate regions of positive climb force (green) from negative climb force (blue). A detailed description of the figure is given in Section 3.1. (For interpretation of the references to color in this figure legend, the reader is referred to the web version of this article.)

was used rather than Eq. (1) to determine the position at which the sign of the vacancy chemical potential changes.

Four dislocation glide planes are drawn at the left (approach) side of Fig. 3 as dashed horizontal lines. At glide plane I ( $z_o/R = 0.8$ ), the dislocation glides toward the precipitate (positive  $y$  direction) under an applied shear stress equal to  $1/8$  of the Orowan stress ( $\sigma_{Or}/8 = [31.3\text{ MPa}]/8 = 3.9\text{ MPa}$ ). This glide plane is in the top left glide force sector ( $y_o/R < 0$ ;  $z_o/R > 0.5$ ) where precipitate-induced glide forces on the dislocation are positive, i.e. the dislocation is attracted by the precipitate by the glide forces it induces. Then, the glide force which acts on the dislocation is larger than the externally applied force, i.e. the applied force and the precipitate force have the same sign. The dislocation glide continues until, after crossing the  $f_{Or} = 0$  boundary, it stops at point  $i$  at the  $-f_{Or}/8$  glide force contour, at which position the glide forces on the dislocation due to the applied stress  $f_{Or}/8$  and to the precipitate (from lattice and modulus mismatch)  $-f_{Or}/8$  are balanced. At point  $i$ , the negative glide force contours are essentially compressed into a single curve. From here, due to the repulsive interaction force of the precipitate, the dislocation cannot glide further on the same plane, and must climb to bypass it. The trajectory of a positively climbing dislocation is highlighted in red in Fig. 3. Due to the adsorption of vacancies, the dislocation climbs up over the precipitate while gliding to remain on the  $-f_{Or}/8$  glide force contour (in a clockwise direction in Fig. 3) until it reaches point  $T$ . Here the dislocation becomes trapped, for reasons explained in detail below.

At glide plane II ( $z_o/R = 0$ ), the dislocation glides toward the precipitate as described above at plane I. In this case, however, since the glide plane is in the lower left glide force sector, where the precipitate-induced glide forces act in the negative  $y$ -direction (i.e. the dislocation is repelled by the precipitate), the net glide force on the dislocation as it approaches the  $-f_{Or}/8$  glide force contour is smaller than  $f_{Or}/8$ . The dislocation encounters the  $-f_{Or}/8$  glide force contour at point  $ii$ , and follows the same path to point  $T$  where it is trapped, as described above for plane I.

At glide plane III ( $z_o/R = -1.2$ ), the dislocation again glides to the  $-f_{Or}/8$  contour (point  $iii$ ), where, because the vacancy chemical potential is still negative, vacancies are adsorbed, allowing the dislocation to climb up, in the  $z > 0$  direction. This case is distinct from glide planes I and II, because climb over the precipitate requires that the dislocation travels first in the negative  $y$ -direction, against the applied shear stress, before passing point  $V$  where the slope  $dz/dy$  of the climb trajectory is infinite. The driving force for climb between points  $iii$  and  $V$  is provided by the climb interaction force, which is positive here. As for cases I and II, the dislocation climbs to point  $T$  and becomes trapped.

At glide plane IV ( $z_o/R = -1.7$ ) the dislocation encounters the  $-f_{Or}/8$  glide force contour at point  $iv$ . The sign of the chemical potential is positive here, so the dislocation climbs down due to vacancy emission, moving counterclock-

wise under the precipitate until point *E* where the slope  $dz/dy$  of the climb trajectory is zero. At *E*, therefore, the dislocation is able to escape the precipitate, since by gliding past this point along the blue horizontal dashed line that begins at *E*, the dislocation moves down a gradient of glide forces provided by the mismatching precipitate, i.e. the dislocation is repelled.

### 3.2. Model refinements

Two modifications were made to the M–D model in its reimplementation. First, in the M–D model [11], the approach angle,  $\beta = \tan^{-1}(dz/dy)$ , was taken to be that of a dislocation following a semicircular path of radius equal to the precipitate radius, *R*. In fact, the dislocation trajectory is more complex (Fig. 3). Eq. (1) indicates that correct treatment of this angle,  $\beta$ , is important as it determines what fraction of the climb force is resolved onto the dislocation trajectory. Furthermore,  $\beta$  appears in both  $(\partial l/\partial y)_{ABC}$  and in  $dA_{AB}/dy$ ; the full expressions for these quantities are derived in Ref. [13]. Secondly, according to Eq. (1), a negative glide force,  $F_g < 0$ , increases the chemical potential of a vacancy  $\mu_v$ , reducing the driving force for dislocation climb over the precipitate. This implies that for a unit advance  $\delta y$ , the dislocation requires an energy per unit length  $-F_g \delta y$ , which increases  $\mu_v$ . In other words, adding a vacancy to the climbing dislocation allows it to glide forward, but this glide raises the system energy. This is an important and incorrect departure from the treatment in the R–A model [13], in which the applied shear stress drives the dislocation forward, reducing its energy, and thereby reducing  $\mu_v$ . Therefore, a more nuanced treatment was taken here, as follows: as the dislocation gains vacancies, it climbs from  $(y_o, z_o)$  to  $(y_o, z_o + \delta z)$ ; thereby leaving the trajectory dictated by the equilibrium in glide forces. At height  $z_o + \delta z$ , it is subjected to an imbalance in the net glide forces,  $\Delta F_g = \tau_{yz} b \lambda + F_g(z_o + \delta z)$ , where the externally applied shear stress,  $\tau_{yz}$ , multiplied by the Burgers vector *b*, and the interprecipitate distance  $\lambda$ , is equal to  $-F_g(z_o)$ . The imbalance  $\Delta F_g$  drives the dislocation forward (in the cases I, II and IV above) or backward (in case III) by a distance  $\delta y$  where it rejoins the equilibrium trajectory. Unlike the M–D model [11], the work done on the dislocation by the applied shear stress is always positive when the dislocation glides in the positive *y*-direction, thereby reducing  $\mu_v$  and aiding dislocation climb. Making the approximation that  $F_g$  varies linearly with *y*, the average glide force restoring the dislocation to its equilibrium trajectory between  $(y_o, z_o + \delta z)$  and  $(y_o + \delta y, z_o + \delta z)$  is  $\Delta F_g/2$ . In the present implementation, the climb increment  $\delta z$  was chosen to be equal to the Burgers vector,  $\pm b$ . The resulting expression for  $\mu_v$  becomes:

$$\mu_v = \frac{\frac{\mu_m b^2}{2} \left( \frac{\partial l}{\partial y} \right)_{ABC} - F_c \tan(\beta) - \frac{\Delta F_g}{2}}{\frac{1}{b_2} \frac{\partial A_{AB}}{\partial y}} \quad (3)$$

Whether a dislocation will climb over or under the precipitate depends on the sign of the chemical potential of a vacancy,  $\mu_v$ : a negative value of  $\mu_v$  means that vacancies will diffuse from the matrix to the dislocation, resulting in positive climb (over the particle); a positive value of  $\mu_v$  corresponds to diffusion of vacancies from the dislocation to the matrix, resulting in negative climb (under the particle). Red (blue) arrowheads on the dislocation trajectories at the approach side of the precipitate in Fig. 3 indicate the glide plane height where a dislocation climbs over (under) the precipitate. It is stated in Ref [11] that for dislocations gliding toward the precipitate with initial height  $z_o > 0$ , bypass occurs by climb over the precipitate, while if  $z_o < 0$ , dislocations climb under. Fig. 3 indicates that this is not generally the case.

## 4. Results and discussion

### 4.1. Dislocation trapping at the departure side

Because functioning source code for the M–D model [11] was not available, it was rewritten entirely, in Mathematica version 7.0. The model was run for a 5.9 nm radius  $\text{Al}_3\text{Sc}$  precipitate, in an attempt to reproduce the results in Ref. [11]. Those results, however, could not be reproduced even when the reimplemented model was modified to mimic the treatment of  $\beta$  and  $F_g$  used in Ref. [11]. In the present code implementation, with both the previous and the refined treatment of  $\beta$  and  $F_g$ , dislocation climb over the precipitate is aided by the elastic interactions (i.e. the climb forces due to the precipitates are positive, in the green-shaded region of Fig. 3). Although a number of possible explanations for this discrepancy were explored, we are unable to account for the different results found in the present implementation and in Ref. [11], with or without the refinements on  $\beta$  and  $F_g$ .

In the present implementation, the dislocation behavior was also considered at the departure side, after the dislocation climbed over the precipitate to the position  $(y_o, z_o) = (0, R)$ . At the trapping point *T*, the dislocation is impeded by the departure-side forces such that it can neither climb over nor under them. For the positive climb trajectory, the helpful precipitate-induced climb force is not large enough to compensate for the energy required to produce additional dislocation length and to overcome the externally applied glide force. For the negative climb trajectory, the reduction in dislocation length and the energy gained by gliding forward with the externally applied glide force are insufficient to compensate for the energy required to oppose the precipitate-induced climb force. In other words, point *T* is a position of local equilibrium for the dislocation. The model therefore predicts that the dislocation, after climbing over the mismatching precipitate by vacancy-mediated diffusion, cannot escape the departure side by that mechanism, even though those same interactions aid its climb at the approach side. A creep strain rate due to dislocation climb over elastically

interacting precipitates by vacancy diffusion cannot therefore be predicted by this model, contrary to Ref. [11]. Thermally activated detachment is possible, however, as considered by Arzt and Rösler [37] for the case of a dislocation detaching from the departure-side interface of an incoherent dispersoid. This mechanism is not considered in the present model, which thus represents the “athermal” case.

All experimental creep studies of dilute Al–Sc–X alloys, which contain coherent, mismatching  $\text{Al}_3(\text{Sc},\text{X})$  precipitates [4,5,23–31], report a threshold stress (at which a compressive creep rate for uniaxial compressive stress is not measurable in the laboratory) which increases with precipitate size and lattice parameter mismatch, as shown in Fig. 4. In this figure, experimentally measured uniaxial threshold stresses normalized to a calculated uniaxial Orowan stress increment, are plotted as a function of precipitate radius, determined by atom probe tomography. The uniaxial Orowan stress increment is calculated as  $M\Delta\sigma_{Or}^c$ , where  $M$  (equal to 3.06 for Al [38]) is the mean matrix orientation factor allowing conversion from shear to uniaxial stresses. The lattice parameter mismatch of precipitates in the three systems is smallest in Al–Sc–Li, and largest in Al–Sc–Yb (Table A1). These results support the hypothesis that elastic interactions between dislocations and coherent, misfitting precipitates are responsible for the observed trends in threshold stress behavior for these systems. A

new mechanism to account for threshold stress behavior due to those interactions is therefore presented below.

## 4.2. Glide force-based threshold stress model

### 4.2.1. Glide forces at the precipitate apex

The departure-side forces, as illustrated in Fig. 3 for example, increase in magnitude with both precipitate size and lattice parameter mismatch. For a dislocation that has climbed over the precipitate and become trapped at the departure side (point  $T$  in Fig. 3), a sufficiently large applied shear stress  $\tau_{yz}$  will overcome the attractive departure-side forces, driving the dislocation through the region of elastic interactions, as described below. The dislocation then glides in the positive  $y$ -direction, on the plane indicated by a blue dashed line labeled I–III in Fig. 3. As described above, to escape the precipitate, the dislocation must glide rather than climb, since the forces acting on the dislocation during climb over (under) the region of departure-side interactions do not provide the energy for vacancy adsorption to (emission from) the dislocation.

For the example shown in Fig. 3, the normalized glide force,  $F_g/f_{Or}$ , for a dislocation that climbed to the apex of the  $\text{Al}_3\text{Sc}$  precipitate ( $z_o = R + |b|$ ,  $R = 5$  nm) is shown as a function of the normalized glide distance  $y_o/R$  in Fig. 5. For comparison, Fig. 5 also includes the same curve for  $\text{Al}_3(\text{Sc}_{0.8}\text{Yb}_{0.2})$  and  $\text{Al}_3(\text{Sc}_{0.65}\text{Li}_{0.35})$  precipitates. The curve

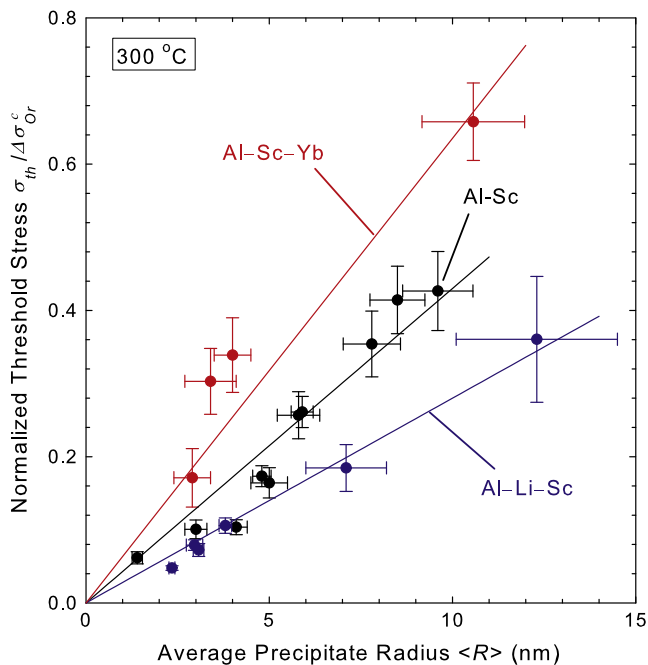


Fig. 4. Plot of experimental creep threshold stress data at 300 °C for Al–Sc [4,5], Al–Sc–Yb [30,39] and Al–Li–Sc [31] alloys vs. average precipitate radii. Straight lines are weighted best fits to the data, but forced to pass through the origin. For the best-fit lines, the data are weighted by the product of the uncertainties in the average precipitate radius and the normalized threshold stress.

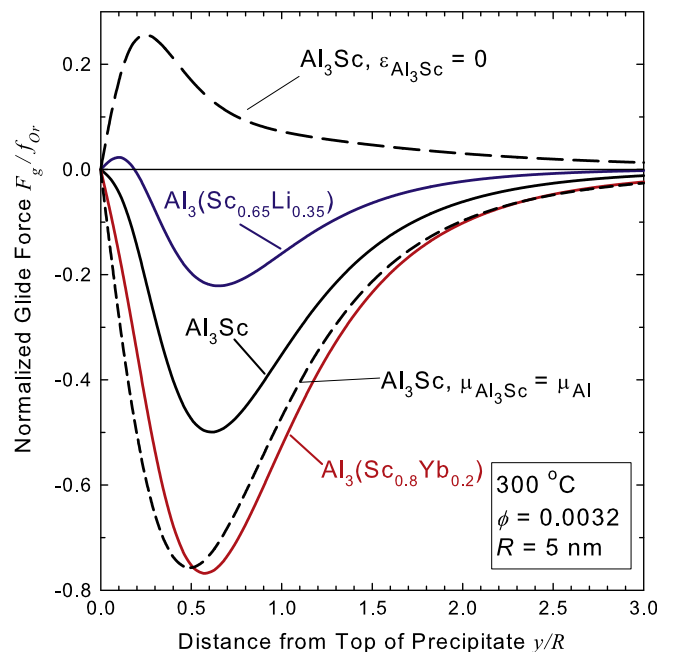


Fig. 5. The glide force on a dislocation, normalized to the glide force from an externally applied shear stress equal to the Orowan stress, as a function of glide distance from  $(0, R + |b|)$  (the “apex” of the precipitate). Curves for  $\text{Al}_3\text{Sc}$ ,  $\text{Al}_3(\text{Sc}_{0.8}\text{Yb}_{0.2})$  and  $\text{Al}_3(\text{Sc}_{0.65}\text{Li}_{0.35})$  precipitates are shown, and their minima correspond to the threshold force. The curve from  $\text{Al}_3\text{Sc}$  is decomposed into its contributions from lattice parameter mismatch (label:  $\text{Al}_3\text{Sc}$ ,  $\mu_{\text{Al}_3\text{Sc}} = \mu_{\text{Al}}$ ) and shear modulus mismatch (label:  $\text{Al}_3\text{Sc}$ ,  $\varepsilon_{\text{Al}_3\text{Sc}} = 0$ ).

for  $\text{Al}_3\text{Sc}$  is decomposed into its two contributions: glide force from lattice parameter mismatch (shorter dashes) and from shear modulus mismatch (longer dashes). For  $\text{Al}_3\text{Sc}$ , the magnitude of the force opposing dislocation glide is greatest at  $y_o \approx 0.6R$ , where it has a value  $F_g/f_{or} \approx -0.5$ . If the force on the dislocation due to the applied shear stress exceeds this critical value (the threshold force), the dislocation escapes the precipitate: thus, the applied stress is equal to the threshold stress. Fig. 5 shows that the glide forces due to shear modulus mismatch repel the dislocation from the precipitate, while glide forces due to lattice parameter mismatch attract the dislocation to the precipitate. Because the effect of lattice parameter mismatch is greater in this particular example, the net effect is that the dislocation is attracted to the departure side of the precipitate. The maximum glide forces needed to escape  $\text{Al}_3(\text{Sc}_{0.8}\text{Yb}_{0.2})$  and  $\text{Al}_3(\text{Sc}_{0.65}\text{Li}_{0.35})$  precipitates are larger and smaller, respectively, than those due to  $\text{Al}_3\text{Sc}$ , in agreement with the same trend in the lattice parameter mismatch with the matrix. For values of  $y_o/R < \sim 0.2$ , the glide force due to  $\text{Al}_3(\text{Sc}_{0.65}\text{Li}_{0.35})$  precipitates is positive (the precipitate repels the dislocation), because the attractive glide force due to lattice strain is smaller than the repulsive glide force due to shear modulus mismatch. As noted above, if the sign on the lattice parameter mismatch is reversed, the stresses in Fig. 2 are mirrored about  $z = 0$ , which results in identical values for the normalized glide forces plotted in Fig. 5.

It is important to note that the departure-side threshold force (and thus stress) predicted by these results has a different origin to the departure-side detachment stresses predicted by models considering the reduction in dislocation line energy at the incoherent dispersoid–matrix interface [8,9,19–22]. The threshold force predicted by the present model does not consider any interaction with the coherent precipitate–matrix interface, but only the mismatch stresses induced in the matrix as described above.

#### 4.2.2. Constraints on the dislocation geometry

The constraints in the present model (segment AB must remain straight; cross-slip and bypass by Orowan looping are not allowed) have implications on the stress required for a dislocation to bypass a precipitate. Using a dislocation dynamics model without these constraints, the behavior of an edge or screw dislocation climbing over a size-mismatched precipitate was investigated in detail by Xiang and Srolovitz (X–S) [40]. In that work, interactions between the dislocation and a periodic three-dimensional array of size-mismatched spherical precipitates were simulated; shear modulus-mismatch was not, however, considered. An applied shear stress caused the dislocation to advance towards a precipitate. The dislocation glided under the action of a low (160 MPa) or a high (640 MPa) applied shear stress. In some cases, the dislocation was allowed to climb as well. The glide and climb velocities were related linearly to the glide and climb forces on the dislocation, through glide and climb mobilities, respec-

tively, which had the ratio  $m_c/m_g = 0.1$  in most cases. With climb allowed, it was found that, at low stresses, dislocations bypassed precipitates by climb, while at high stresses they bypassed precipitates by a combination of climb, looping and cross-slip. Climb lowered the stress at which dislocations bypass precipitates, at both low and high applied stresses.

Of particular relevance to the present model are the predicted configurations of dislocations climbing past size-mismatched precipitates in the X–S model [40]. The geometry relating the dislocation and precipitate are reversed from the present case, so that positive heights ( $z_o > 0$ ) in the present work correspond to negative heights ( $z_o < 0$ ) in Ref. [40] (i.e. the apex of the precipitate in Fig. 2 here is equivalent to the nadir of the precipitate in Fig. 4 of Ref. [40]). That figure shows an equilibrium configuration of an edge dislocation that climbed in the negative direction, to the nadir of a precipitate—equivalent to the position  $(0, R)$  in the present work—under a low applied stress. Although the mobilities used in the X–S model [40] do not have a physical basis, such as the vacancy chemical potential used in the present simulation, the same behavior is found in both simulations: for low stresses, the dislocation is unable to overcome the glide forces due to size mismatch, which oppose its detachment from the precipitate. Although a screw dislocation is not modeled in the present work, in the X–S model [40] it was found that, for the same low stress, screw dislocations do not bypass the precipitate either, although they exhibit more complex behavior resulting in helices surrounding the precipitate.

The fact that three-dimensional dislocation behavior is fully allowed for in the X–S model [40], and not in the present simulation, has important consequences for the behavior of a dislocation as it frees itself from the trapping point  $T$ . As is shown in Fig. 5 of Ref. [40], when a sufficiently large stresses was applied to a climbing edge dislocation trapped at this position, it escaped by a combination of climb, looping and cross-slip, leaving behind a prismatic dislocation loop in the  $y$ – $z$  plane (equivalent to the  $x$ – $z$  plane in Fig. 2). This is an example of threshold stress behavior due to dislocation climb over an elastically interacting, size-mismatched precipitate that is not sheared. Complex dislocation motion of this type was not modeled in the present work but if this behavior were included in the present simulation, the applied shear stress necessary to cause the dislocation to escape the precipitate–interaction forces at the departure-side would be reduced, similar to the way in which Orowan looping reduces the stress necessary for gliding dislocations to bypass precipitates in an overaged alloy. A final important result of the X–S model [40] is that an edge dislocation was impeded by a size-mismatched precipitate, even when the glide plane did not intersect the precipitate. As described above and as shown in Fig. 2, the present model also accounts for the fact that the interaction forces extend out into the matrix, increasing the effective size of the precipitate. Fig. 6 of Ref. [40] shows a climbing edge dislocation that glides past a

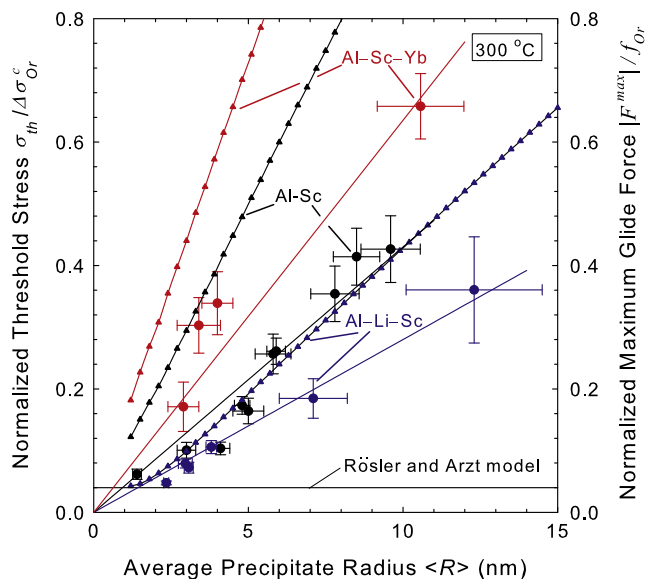


Fig. 6. Right abscissa: the calculated maximum normalized dislocation glide force (threshold force) necessary to overcome departure-side interactions with coherent, misfitting precipitates (small triangles) increases with precipitate radius, and with the magnitude of the mismatch. Left abscissa: experimentally measured normalized threshold stresses (larger circles), repeated from Fig. 4. The horizontal line represents the prediction from the R–A model [13] without elastic interactions between the dislocation and the precipitate.

precipitate at a height of  $1.25 R$ . Although the precipitate is not directly encountered by the dislocation, the strain field in the matrix due to the size-mismatched precipitate is still an obstacle to it. An Orowan loop surrounds the interaction region, whose screw segments then proceed to cross-slip down the sides of the precipitate, leaving behind a prismatic loop similar to that described above.

#### 4.2.3. Comparison with experimentally measured threshold stresses

Although the normalized (dimensionless) threshold force values obtained in the present calculations are larger than experimentally measured normalized (dimensionless) threshold stresses, the maximum precipitate-induced attractive force felt by a dislocation is an increasing function of both precipitate radius and lattice parameter mismatch, in accord with the threshold stress behavior experimentally measured in Al–Sc–X (X = RE, Li or TM) alloys. Fig. 6 displays the maximum glide force induced by  $\text{Al}_3(\text{Sc}_{1-y}\text{X}_y)$  precipitates (i.e. the threshold force) as a function of  $R$ , at a glide plane height  $z_o = R + |b|$ , for a volume fraction of 0.0032. Three types of precipitates are included in the plot:  $\text{Al}_3\text{Sc}$  embedded in a pure Al matrix [4,5],  $\text{Al}_3(\text{Sc}_{0.8}\text{Yb}_{0.2})$  in a pure Al matrix [30,39], and  $\text{Al}_3(\text{Sc}_{0.65}\text{Li}_{0.35})$  in a matrix of Al–2.9 Li (at.%) [41]. Values of the lattice parameters and elastic constants of Al–Sc, Al–Sc–Yb and Al–Li–Sc alloys are given in the Appendix, as is a description of the methodology used to determine them.

Model results for the normalized threshold force in Fig. 6 bear important similarities to a plot of the experimentally measured normalized threshold stress, Fig. 4,

which is superimposed on Fig. 6. In both cases the normalized threshold force and stress increase nearly linearly with  $R$ . Also, in both cases, precipitates having a larger lattice parameter mismatch with the matrix also have larger normalized stresses (forces). As described above, the geometry of the individual precipitate, the arrangement of all precipitates, and the shape of the climbing dislocation are all more complex than the model, which may account for the larger normalized force values predicted by it. Although the M–D model results were based on a kinetically informed methodology of determining the threshold stress [11], the same quasi-linear dependence of threshold stress on  $R$ , increasing also with lattice parameter mismatch, was predicted there as well.

The similarities between the dependence of threshold forces due to misfitting precipitates, and threshold stresses measured in creep experiments, suggest that stress-driven departure-side escape of dislocations plays a controlling role in the threshold stress behavior of alloys strengthened by coherent, misfitting precipitates. This mechanism for threshold stresses is a departure from the one explored in the R–A and M–D models [11,13], which was due to an applied-stress-induced increase in the driving force for the adsorption of vacancies onto the dislocation, i.e. the magnitude of the vacancy chemical potential, which enabled appreciable rates of climb over the particle. Hence, the present model does not account in any way for the kinetics of dislocation climb; it is therefore not possible to compute strain rate vs. stress curves, as was done in the R–A and M–D models [11,13]. It is, however, possible to calculate the force (normalized to the Orowan force) necessary to overcome departure-side interaction stresses for coherent, misfitting precipitates. The present model predicts normalized force values close to the experimentally measured normalized threshold stresses in Al–Sc–X alloys, as shown in Fig. 6. The threshold value is over-predicted because the dislocation shape is constrained in a way that excludes lower-stress escape trajectories, which are predicted by the X–S model [40].

It should be possible to bring more sophisticated techniques to bear on this problem. For example, three-dimensional dislocation dynamics models such as the X–S model described above [40], or two-dimensional ones such as those in Refs. [42,43] could be used to calculate a threshold stress based on more realistic geometries, including spherical precipitates with spatial arrangements and size distributions derived from experiments, and complex configurations for a dislocation propagating across a glide plane. Such an approach would still fail to predict any kinetic feature of creep by dislocation climb, but may provide more accurate values for the normalized threshold stress than those presented here.

## 5. Summary

A model by Rösler and Arzt [13] for creep in alloys strengthened by coherent, unsharable precipitates by

general climb of dislocations over obstacles was extended by Marquis and Dunand [11] to include elastic interactions between the dislocation and the precipitate due to matrix–precipitate mismatch in lattice parameter and shear modulus. Creep threshold stresses in Al strengthened by Al<sub>3</sub>Sc precipitates were calculated by the M–D model [11], in semiquantitative agreement with experimental results. This extended model is revisited in the present work. The source code for the model was rewritten, and two inaccuracies were corrected, yielding the following conclusions:

1. The basic result from the M–D model [11]—that elastic interactions between dislocations and Al<sub>3</sub>Sc precipitates result in threshold stresses due to a stress-dependent reduction in the dislocation climb rate—could not be reproduced. This was true whether or not the differences between the M–D model and the present treatment [11] were mimicked in the new code. In the present implementation, elastic interactions were found to aid dislocation climb over the precipitate.
2. In the present model, the dislocation that climbs to the apex of a precipitate by vacancy-mediated diffusion becomes trapped close to this position by stresses induced in the matrix by the lattice-parameter-mismatching precipitate. The dislocation cannot escape the precipitate, as it can climb neither over nor under the region of departure-side stresses. Only the application of an externally applied stress (the threshold stress) produces a shear force (the threshold force) that allows for escape of the dislocation. An escape stress by a similar mechanism has been predicted by Xiang and Srolovitz using a more sophisticated dislocation dynamics simulation [40] wherein a dislocation climbs in three dimensions over a misfitting spherical particle. The threshold stress modeled in the present work is distinct from interface-related detachment stresses such as those postulated for dislocation climb and bypass of incoherent dispersoids [8,9,19–22].

3. The magnitude of the threshold force (normalized to the Orowan force) necessary to effect dislocation escape increases with the magnitude of the precipitate lattice parameter mismatch, and with its radius  $R$ . This behavior is qualitatively similar to experimental measurements of creep threshold stresses (normalized to the Orowan stress) in Al–Sc–X alloys and to the results presented in Ref. [11]. Although the normalized threshold stress (force) increases with  $R$ , the Orowan stress decreases with  $R$ . Thus, increasing the lattice parameter mismatch of precipitates is a better strategy for improving creep resistance than increasing  $R$ .
4. The present model suggests that the creep threshold stresses in alloys strengthened by coherent misfitting precipitates may be due to the requirement that the internal stress between dislocations and precipitates be overcome, and not due to a requirement that a sufficient driving force for vacancy diffusion to the climbing precipitate be supplied.

### Acknowledgments

This research is supported by the US Department of Energy, Office of Basic Energy Sciences through Grant DE-FG02-98ER45721 (Dr. J. Vetrano, monitor). The authors thank Dr. R.A. Karnesky (Sandia National Laboratory), Prof. E.A. Marquis (University of Michigan, Ann Arbor) and Prof. D.N. Seidman (Northwestern University) for numerous useful discussions. The authors also thank Dr. Zungang Mao (Northwestern University) for performing first-principles calculations.

### Appendix A. lattice parameters and elastic constants of Al–Sc, Al–Sc–Yb and Al–Li–Sc alloys

The compositions of Al<sub>3</sub>Sc, Al<sub>3</sub>(Sc, Li) and Al<sub>3</sub>(Sc, Yb) precipitates are taken to be uniform, although in fact

Table A1

Constants used in the calculations of interaction forces between dislocations and precipitates at 300 °C.

Property	Value	Ref.
Constrained lattice parameter mismatch [%]		
Al <sub>3</sub> Sc	0.72	[44]
Al <sub>3</sub> (Sc <sub>0.8</sub> Yb <sub>0.2</sub> )	0.98	[52]
Al <sub>3</sub> (Sc <sub>0.65</sub> Li <sub>0.35</sub> )	0.36	[43,45]
Burgers vector [nm]		
Al, Al–2.9 at.% Li	0.288	[44,50]
Shear modulus [GPa]		
Al <sub>3</sub> Sc, Al <sub>3</sub> (Sc <sub>0.8</sub> Yb <sub>0.2</sub> ) <sup>a</sup>	68.4	[46]
Al <sub>3</sub> (Sc <sub>0.65</sub> Li <sub>0.35</sub> ) <sup>a</sup>	59.2	[46–48]
Al	21.7	[50]
Al–2.9 at.%Li	23.8	[48,50]
Poisson's ratio [-]		
Al <sub>3</sub> Sc, Al <sub>3</sub> (Sc <sub>0.8</sub> Yb <sub>0.2</sub> ), Al <sub>3</sub> (Sc <sub>0.65</sub> Li <sub>0.35</sub> ) <sup>a</sup>	0.22	[46, 47]
Al, Al–2.9 at.%Li <sup>a</sup>	0.34	[47]

<sup>a</sup> Ambient temperature value is used.

$\text{Al}_3(\text{Sc}_{0.8}\text{Yb}_{0.2})$  precipitates exhibit a core–shell structure, with a Yb-rich core and a Sc-rich shell [30,39]. The constrained lattice parameter mismatches are calculated at 300 °C as described in Ref. [44], taking the coefficients of thermal expansion of precipitates and matrix to be equal to those of  $\text{Al}_3\text{Sc}$  and pure Al, respectively. For  $\text{Al}_3(\text{Sc}_{0.65}\text{Li}_{0.35})$  precipitates, the lattice parameter is determined based on a first-principles calculation [45] as described in Ref. [43], and the shear modulus is calculated by interpolating between the shear moduli of  $\text{Al}_3\text{Sc}$  [46,47] and  $\text{Al}_3\text{Li}$  [48]. The  $\text{Al}_3(\text{Sc}_{0.65}\text{Li}_{0.35})$  precipitate is modeled as being embedded in an Al-2.9 Li (at.%) matrix [41], whose lattice parameter varies negligibly due to the dissolved Li [49], and whose shear modulus is somewhat increased by it [48]. The temperature dependence of the matrix shear modulus is calculated according to Ref. [50], while the temperature dependence of the precipitate shear moduli, and of the matrix and precipitate Poisson's ratios are unknown, and thus are not accounted for. For  $\text{Al}_3(\text{Sc}_{0.8}\text{Yb}_{0.2})$ , the lattice parameter is determined using a Vegard's law dependence to interpolate between  $\text{Al}_3\text{Sc}$  [51,52] and  $\text{Al}_3\text{Yb}$  [52], and the shear modulus of the precipitate is taken to be equal to that of  $\text{Al}_3\text{Sc}$ . The Poisson's ratio for all precipitates is taken to be that of  $\text{Al}_3\text{Sc}$  [46,47]. Values for the parameters used in the model are presented in Table A1.

## References

- [1] Cadek J. Creep in precipitation and dispersion strengthened alloys. Creep in metallic materials, vol. 11. Amsterdam: Elsevier; 1988. p. 176.
- [2] Nabarro RN, Villiers HLd. The physics of creep: creep and creep-resistant alloys. London: Taylor & Francis; 1995.
- [3] Lagneborg R, Bergman B. Metal Sci 1976;10:20.
- [4] Marquis EA, Seidman DN, Dunand DC. Acta Mater 2003;51:285.
- [5] Seidman DN, Marquis EA, Dunand DC. Acta Mater 2002;50:4021.
- [6] Stevens RA, Flewitt PEJ. Acta Metall 1981;29:867.
- [7] Blum W, Reppich B. Creep of particle-strengthened alloys. In: Evans RW, Wilshire B, editors. Creep behaviour of crystalline solids, vol. 3. Aldershot: Ashgate Publishing; 1985. p. 83.
- [8] Nardone VC, Matejczyk DE, Tien JK. Acta Metall 1984;32:1509.
- [9] Srolovitz D, Petkovicluton R, Luton MJ. Scripta Metall 1982;16:1401.
- [10] Deshmukh SP, Mishra RS, Robertson IM. Mater Sci Eng A 2010;527:2390.
- [11] Marquis EA, Dunand DC. Scripta Mater 2002;47:503.
- [12] Nardone VC, Tien JK. Scripta Metall 1983;17:467.
- [13] Rösler J, Arzt E. Acta Metall 1988;36:1043.
- [14] Brown LM, Ham RK. Dislocation-particle interactions. In: Kelly A, Nicholson RB, editors. Strengthening methods in crystals. Amsterdam: Elsevier; 1971. p. 9–135.
- [15] Shewfelt RSW, Brown LM. Philos Mag 1977;35:945.
- [16] Hausselt JH, Nix WD. Acta Metall 1977;25:1491.
- [17] Lagneborg R. Scripta Metall 1973;7:605.
- [18] Arzt E, Ashby MF. Scripta Metall 1982;16:1285.
- [19] Srolovitz DJ, Petkovicluton RA, Luton MJ. Philos Mag A 1983;48:795.
- [20] Srolovitz DJ, Petkovicluton RA, Luton MJ. Acta Metall 1983;31:2151.
- [21] Arzt E, Wilkinson DS. Acta Metall 1986;34:1893.
- [22] Mishra RS, Nandy TK, Greenwood GW. Philos Mag A 1994;69:1097.
- [23] Fuller CB, Seidman DN, Dunand DC. Acta Mater 2003;9951:4803.
- [24] Karnesky RA, Seidman DN, Dunand DC. Mater Sci Forum 2006;519–521:1035.
- [25] Marquis EA, Seidman DN, Dunand DC. Acta Mater 2003;51:4751.
- [26] Knipling KE, Dunand DC. Scripta Mater 2008;59:387.
- [27] van Dalen ME, Dunand DC, Seidman DN. Acta Mater 2005;53:4225.
- [28] van Dalen ME, Seidman DN, Dunand DC. Acta Mater 2008;56:4369.
- [29] Knipling KE, Seidman DN, Dunand DC. Acta Mater 2011;59:943.
- [30] van Dalen ME, Dunand DC, Seidman DN. Acta Mater 2011;59:5224–37.
- [31] Krug ME, Seidman DN, Dunand DC. Acta Mater 2011, submitted for publication.
- [32] Dundurs J. Elastic interaction of dislocations with inhomogeneities. In: Mura T, editor. Mathematical theory of dislocations. New York: American Society of Mechanical Engineers; 1969. p. 70.
- [33] Dundurs J, Mura T. J Mech Phys Solids 1964;12:177.
- [34] Eshelby JD. Proc Roy Soc London 1957;A241:376.
- [35] Peach M, Koehler JS. Phys Rev 1950;80:436–9.
- [36] Nembach E. Particle strengthening of metals and alloys. New York: Wiley-Interscience; 1996.
- [37] Arzt E, Rösler J. Acta Metall 1988;36:1053.
- [38] Meyers MA, Chawla KK. Mechanical metallurgy: principles and applications. Englewood Cliffs, NJ: Prentice-Hall; 1984.
- [39] van Dalen ME. Microstructure and creep properties of Al–Sc alloys micro-alloyed with lanthanides (Yb or Gd) and transition metals (Ti or Zr). Ph.D. Thesis, Northwestern University; 2007.
- [40] Xiang Y, Srolovitz DJ. Phil Mag 2006;86:3937.
- [41] Krug ME, Dunand DC, Seidman DN. Acta Mater 2011;59:1700.
- [42] Mohles V. Phil Mag A 2001;81:971.
- [43] Krug ME, Seidman DN, Dunand DC, in preparation.
- [44] Royset J, Ryum N. Scripta Mater 2005;52:1275.
- [45] Mao Z. Personal Communication 2011.
- [46] George EP, Horton JA, Porter WD, Schneibel JH. J Mater Res 1990;5:1639.
- [47] Hyland Jr RW, Stiffler RC. Scr Metall Mater 1991;25:473.
- [48] Mueller W, Bubek E, Gerold M. Elastic constants of Al–Li alloys and  $\delta'$  precipitates. In: Baker C, Gregson PJ, Harris SJ, Peel CJ, editors. Aluminium–lithium alloys III. Oxford; 1985. p. 435.
- [49] Levine E, Rapperport E. Trans Metall Soc AIME 1963;227:1204.
- [50] Frost HJ, Ashby MF. Deformation-mechanism maps. Oxford: Pergamon Press; 1982.
- [51] Murray JL. J Phase Equilib 1998;19:380–4.
- [52] Knipling KE, Dunand DC, Seidman DN. Zeitschrift für Metallkunde 2006;97:246.